

# Two-dimensional XY ferromagnetism above room temperature in Janus monolayer $V_2XN$ ( $X = P, As$ )

Wenhui Wan,<sup>a</sup> Botao Fu,<sup>b</sup> Chang Liu,<sup>c</sup> Yanfeng Ge,<sup>a</sup> and Yong Liu<sup>\*a</sup>

<sup>a</sup>State Key Laboratory of Metastable Materials Science and Technology & Key Laboratory for Microstructural Material Physics of Hebei Province, School of Science, Yanshan University, Qinhuangdao, 066004, P. R. China

<sup>b</sup>College of Physics and Electronic Engineering, Center for Computational Sciences, Sichuan Normal University, Chengdu, China

<sup>c</sup>Institute for Computational Materials Science, Joint Center for Theoretical Physics (JCTP), School of Physics and Electronics, Henan University, Kaifeng, 475004, China.

E-mail: yongliu@ysu.edu.cn

July 2022

**Abstract.** Two-dimensional (2D) XY magnets with easy magnetization planes support the nontrivial topological spin textures whose dissipationless transport is highly desirable for 2D spintronic devices. Here, we predicted that Janus monolayer  $V_2XN$  ( $X = P, As$ ) with a square lattice are 2D-XY ferromagnets by first-principles calculations. Both the magnetocrystalline anisotropy and magnetic shape anisotropy favor an in-plane magnetization, leading to an easy magnetization  $xy$ -plane in Janus monolayer  $V_2XN$ . Resting on the Monte Carlo simulations, we observed the Berezinskii-Kosterlitz-Thouless (BKT) phase transition in monolayer  $V_2XN$  with transition temperature  $T_{BKT}$  being above the room temperature. Especially, monolayer  $V_2AsN$  has a magnetic anisotropy energy (MAE) of  $292.0 \mu\text{eV}$  per V atom and a  $T_{BKT}$  of 434 K, which is larger than that of monolayer  $V_2PN$ . Moreover, a tensile strain of 5% can further improve the  $T_{BKT}$  of monolayer  $V_2XN$  to be above 500 K. Our results indicated that Janus monolayer  $V_2XN$  ( $X = P, As$ ) were candidate materials to realize high-temperature 2D-XY ferromagnetism for spintronics applications.

*Keywords:* Magnetic semiconductor, Curie temperature, Correlation function, Strain effect.

## 1. Introduction

It had been demonstrated that the long-range magnetic order can exist in two-dimensional (2D) ferromagnetic (FM) materials with an easy magnetization axis including 2D  $\text{CrI}_3$ , [1]  $\text{Fe}_3\text{GeTe}_2$ , [2]  $\text{Cr}_2\text{Ge}_2\text{Te}_6$ , [3]  $\text{MnSe}_2$ , [4] and  $\text{VSe}_2$ . [5] On the

other side, 2D FM materials with an easy magnetization plane, which are called 2D-XY FM materials, exhibit a quasi-long-range order that is described by Berezinskii-Kosterlitz-Thouless (BKT) phase transition. [6] 2D-XY FM materials hold the formation of bound pairs of topological nontrivial meron and antimeron spin textures, which are promising for developing high-speed, low-power, and multi-functional spintronic devices and energy-efficient nanoelectronic devices. [7] The material realization of 2D-XY ferromagnets with a high transition temperature ( $T_{\text{BKT}}$ ) is a fast-developing field and remains a challenge.[8]

2D-XY ferromagnetism had been investigated in 2D hexagonal systems. In the experiment, Tokmachev et al. observed that the sub-monolayer of Eu atoms self-assembled on the silicon surface, [9] graphene, [10] silicene, [11] and germanene [12] exhibited an easy magnetization plane. However, the corresponding transition temperature  $T_{\text{BKT}}$  of Eu-based systems are smaller than 20 K.[9, 10, 11, 12] Pinto et al. demonstrated a BKT phase transition in monolayer  $\text{CrCl}_3$  grown on graphene/6H-SiC(0001) substrate with a  $T_{\text{BKT}}$  of 12.95 K. [13] On the theoretical side, Lu et al. [14] and Augustin et al. [15] investigated the spin textures and dynamics properties of meron and antimeron in 2D-XY magnet monolayer  $\text{CrCl}_3$ . They found that the easy magnetization plane in  $\text{CrCl}_3$  are formed due to competition between the weak out-of-plane single-ion anisotropy and strong in-plane shape anisotropy, as well as the exchange competition between different neighbors, which leads to a low  $T_{\text{BKT}}$  of monolayer  $\text{CrCl}_3$ . [14, 15] Meanwhile, these topologically non-trivial spin textures are robust to external static magnetic field. [14] Strungaru et al. reported the formation and control of merons and antimerons in monolayer  $\text{CrCl}_3$  by the laser pulse via the two-temperature model.[16] Besides  $\text{CrCl}_3$ , easy-plane magnetism has also been predicted in monolayer  $\text{CrAs}$  with a  $T_{\text{BKT}}$  of 855 K, [17] monolayer  $\text{VSi}_2\text{N}_4$  with a  $T_{\text{BKT}}$  of 307 K, [18] and monolayer  $\text{FeX}_2$  ( $\text{X} = \text{Cl}, \text{Br}, \text{and I}$ ) with a maximum  $T_{\text{BKT}}$  of 210 K.[19] However, the  $T_{\text{BKT}}$  of these monolayers [17, 18, 19] has large uncertainty because they were simply estimated by a classical XY model which only considers the nearest-neighbor magnetic coupling and constraints the spin vectors in the  $xy$ -plane. [20] The 2D-XY ferromagnetism in 2D hexagonal systems motivates the search for easy magnetisation plane in other 2D crystal systems. In 2022, Xuan et al. analyzed the 166 stable tetragonal monolayer MX ( $\text{M} = \text{transition metal}, \text{X} = \text{nonmetal}$ ) and found that sufficiently strong M-d/X-p and M-d/M-d couplings can stabilize monolayer MX with the square lattice without ferroelastic transition. [21] For example, monolayer VN adopted a square lattice, while monolayer VP and VAs exhibited a rectangular lattice with ferroelasticity. [22, 23] However, it had not been reported that 2D square lattices have 2D-XY ferromagnetism.

Since the synthesis of Janus  $\text{MoSSe}$  [24] and  $\text{WSSe}$ , [25] the symmetry breaking in the vertical direction of 2D Janus structures can introduce extraordinary physics properties. [26, 27, 28, 29, 30, 31] For example, Janus monolayer  $\text{Cr(I, X)}_3$  ( $\text{X} = \text{Cl}, \text{Br}$ ) and Janus monolayer  $\text{MnXTe}$  ( $\text{X} = \text{S}, \text{Se}$ ) exhibit strong spin-orbit coupling (SOC) and Dzyaloshinskii-Moriya interactions (DMIs) due to the structural symmetry breaking

in the vertical direction, which leads to the intrinsic domain wall skyrmions or the magnetic-field-induced bimerons. [32, 33] Compared to monolayer 2H-VSe<sub>2</sub> which is not stable, Janus monolayer 2H-VSSe, 2H-VSeTe, and 2H-VSTe show a structural stability, an easy magnetization plane, and a  $T_{\text{BKT}}$  of 106 K, 82 K, and 46 K, respectively. [34] Though monolayer CrI<sub>3</sub> is an FM semiconductor with the perpendicular magnetic anisotropy, Janus monolayer Cr<sub>2</sub>I<sub>3</sub>Cl<sub>3</sub> exhibits in-plane magnetic anisotropy. [29] Thus, constructing Janus structures in 2D square systems may be a possible way to realize the easy-plane magnetism.

In this work, based on V-based tetragonal monolayers, we predicted that Janus monolayer V<sub>2</sub>XN ( $X = \text{P, As}$ ) exhibited a 2D square lattice and 2D-XY ferromagnetism by first-principles calculations. We first identified that the FM state was the magnetic ground state for Janus monolayer V<sub>2</sub>XN. Its structural stability was proved by the formation energy, phonon dispersion, thermodynamic studies, and Born criteria. Then, the calculations of magnetic anisotropy energy (MAE) displayed that an easy magnetization plane existed in monolayer V<sub>2</sub>XN. The  $T_{\text{BKT}}$  was estimated by critical behavior of in-plane susceptibility by the Monte Carlo (MC) simulation based on the XXZ model. At last, we found that tensile strain can further enhance the  $T_{\text{BKT}}$  but have a small influence on the MAE.

## 2. Computational method

The first-principles calculations were performed by the Vienna ab initio simulation package (VASP) [35] with the projector augmented wave (PAW) [36] pseudopotentials and Perdew, Burke, and Ernzerhof (PBE) [37] exchange-correlation functionals. A vacuum layer of 20 Å was adopted to prevent artificial interaction between the adjacent periodic images in the  $z$ -direction. The kinetic energy cutoff was set to 550 eV. A  $\mathbf{k}$ -point mesh of  $12 \times 12 \times 1$  with the Monkhorst-Pack scheme [38] was used for the Brillouin zone (BZ) of the primitive cell. The criteria of total energy and atomic force was  $10^{-6}$  eV and  $10^{-3}$  eV/Å, respectively. To appropriately describe the on-site Coulomb repulsion of the localized  $d$  electrons of V atoms, we applied a simplified PBE+U approach proposed by Dudarev et al. [39] An effective Hubbard term  $U_f = U - J = 3$  eV was adopted for V- $d$  orbitals. In previous works,  $U_f = 2 \sim 4$  eV [40, 41, 42, 22] for V- $d$  orbitals had been adopted. We found that the different values of  $U_f$  will not change our main conclusions. The band structures were further checked by Heyd-Scuseria-Ernzerhof (HSE06) hybrid functional. [43] Through the convergence test, the MAE was calculated by a dense  $\mathbf{k}$  mesh of  $30 \times 30 \times 1$  with the SOC effect being included. Phonon dispersion was calculated by a  $5 \times 5 \times 1$  supercell by the density functional perturbation theory implemented in phonopy codes. [44] A  $4 \times 4 \times 1$  supercell was used to perform the molecular dynamics (MD) simulations in the canonical (NVT) ensemble, up to 5 ps with a time step of 1.0 fs. The MC simulations were performed by a  $180 \times 180 \times 1$  supercell using MCSolver code. [45] We run  $2 \times 10^5$  MC steps per site to reach the thermal equilibrium, followed by  $8 \times 10^5$  MC steps per site for the averaging of magnetization and energies. We have

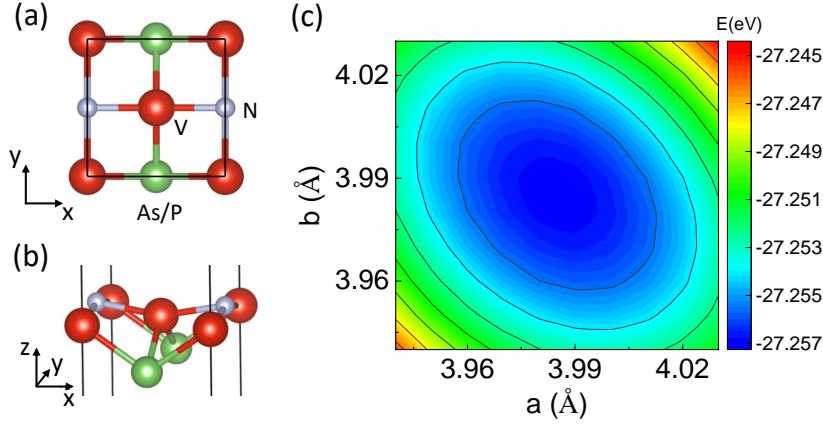


**Figure 1.** (a, b) A top view and a side view of the crystal lattice of Janus monolayer  $V_2XN$  ( $X = P, As$ ). (c) The energy contour of Janus monolayer  $V_2PN$  as a function of lattice constants  $a, b$ . The lattice with  $a = b = 3.986$  Å has the lowest energy.

considered different initial spin configurations concluding spin along the one direction, in the one plane or random direction in 3D space. We got consistent final results that the spins in Janus monolayer  $V_2XN$  ( $X = P, As$ ) tend to form merons and antimerons when the temperature is below the transition temperature  $T_{BKT}$ .

### 3. Results and discussion

We first calculated the intrinsic monolayer VN and VP. Monolayer VP adopted a rectangle lattice with the lattice constants of  $a = 4.219/4.453$  Å and  $b = 3.420/4.443$  Å by PBE/PBE+U calculations. Monolayer VN exhibited a square lattice with the lattice constant of  $a = b = 3.653$  Å and  $3.990$  Å by PBE and PBE+U calculations, respectively. These results agree well with previous works, [22, 23, 46] indicating the reliability of our calculations. Moreover, monolayer VN adopted a buckling and planar structure in the PBE and PBE+U calculations, respectively [see Fig. S1]. Meanwhile, we found that monolayer VN was a non-magnetic (NM) and FM metal in the PBE and PBE+U calculations, respectively. The large difference between the results in PBE and PBE+U calculations indicated the necessity to consider the on-site Coulomb repulsion of the localized  $d$  electrons in both the structural relaxation and electronic structures of V-based materials. In the following content, we only showed the results of PBE+U calculations.

Next, we calculated the energy of monolayer  $V_2XN$  ( $X = P$  and  $As$ ) as a function of the lattice constant. Both monolayer  $V_2PN$  and  $V_2AsN$  adopted 2D square lattice as the lowest-energy lattice structure [see Fig. 1(a-c) and Fig. S2(a)] The corresponding lattice constants are  $a = 3.986$  Å and  $3.989$  Å, respectively. The point group and the space group of monolayer  $V_2XN$  are  $C_{4v}$  and P4mm (No. 99), respectively. There are two V atoms, an N atom, and an X ( $X = P$  and  $As$ ) atom in the primitive cell. In PBE+U calculations, V atoms are located at the 2c (0.5, 0.0, 0.5) Wyckoff sites. The

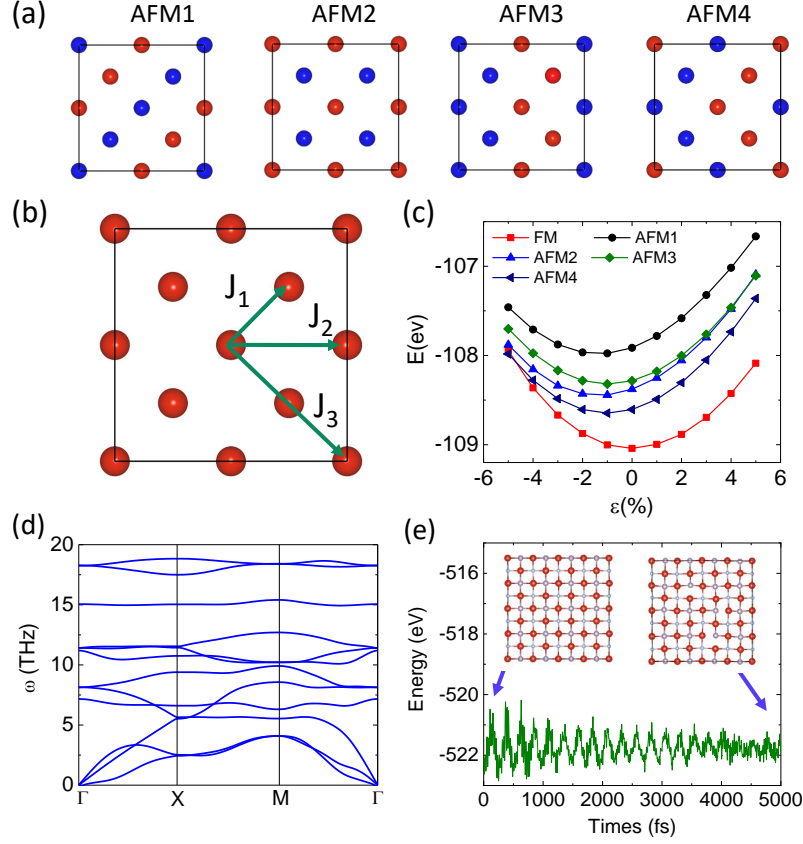


**Figure 2.** (a) Possible AFM states of monolayer  $V_2PN$  with only V atoms being shown. The red and blue balls represent the V atoms with the up and down spins, respectively. (b) FM state and exchange constants  $J_1$ ,  $J_2$ , and  $J_3$ . (c) The energy of monolayer  $V_2PN$  in different magnetic states as a function of biaxial strain. (d) The phonon dispersion of monolayer  $V_2PN$  in the FM state. (e) Evolution of energy of monolayer  $V_2PN$  as a function of time at  $T = 300K$ .

N and X atoms occupy the 1b (0.5, 0.5, 0.5179) and 1a (0.0, 0.0, 0.4313) Wyckoff sites for monolayer  $V_2PN$  and the 1b (0.000, 0.500, 0.5176) and 1a (0.5, 0.0, 0.4216) Wyckoff sites for monolayer  $V_2AsN$ , respectively. Meanwhile, because both the P and As atoms move away from the V-V plane, the V-V distance in monolayer  $V_2XN$  is smaller than that of intrinsic monolayer VN. As a result, both the N side and X side of monolayer  $V_2XN$  experience a compressive strain. We found that the crystal lattice and magnetic properties of  $V_2PN$  and  $V_2AsN$  are similar except that the As atom has a larger buckling height relative to the V-V plane and stronger SOC effect than that of the P atom. We will mainly display the results of monolayer  $V_2PN$  and give the results of monolayer  $V_2AsN$  in the end.

To determine the magnetic ground state of monolayer  $V_2PN$ , we considered it in different magnetic states including the NM state, FM state, and four anti-ferromagnetic (AFM) states by a  $2 \times 2 \times 1$  supercell, as shown in Fig. 2(a, b). We did not display the NM state as its much higher energy than other magnetic states. We defined the biaxial strain as  $\varepsilon = (\frac{a}{a_0} - 1)$ , where  $a$  and  $a_0$  are unstrained and strained lattice constants, respectively.

At  $\varepsilon \leq -5\%$ , an FM-to-AFM phase transition occurs [see Fig. 2(c)]. When  $\varepsilon > -5\%$ , the FM state is the magnetic ground state for monolayer  $V_2PN$  [see Fig. 2(c)]. The V-P-V and V-N-V bonding angles between the nearest V atoms of strain-free monolayer  $V_2PN$  are shown in Table 1. The cation-anion-cation angle is close to  $90.0^\circ$ , which favors an FM coupling between the V atoms according to Goodenough-Kanamori-Anderson superexchange theory. [47] The energy difference between the FM state and AFM states is 0.39 eV for monolayer  $V_2PN$ , indicating a high transition temperature. We also found that the FM state was still the ground state of monolayer  $V_2PN$  for  $U_f = 2$  eV and 4 eV [see Fig. S3]. According to the Hund's rules, each  $V^{3+}$  ion has two unpaired  $d$  electrons with the same spin. The primitive cell with two V ions has a total magnetic moment of  $4 \mu_B$ . From the distribution of spin density, we found that the spin density locates mainly around the V atoms. Charge transfers from the V atoms to the N and P atoms due to the electronegativity difference. Based on the Bader charge analysis, the P atom and N atom get 0.90 e and 1.47 e from V atoms, respectively. The magnetic moments of the V, P, and N ions in a primitive cell are 2.184, -0.224, and -0.255  $\mu_B$ , respectively.

To check the stability of monolayer  $V_2PN$ , we calculated the formation energy by  $E_f = (E_{V_2PN} - 2E_V - E_P - E_N)/4$ , where  $E_{V_2PN}$ ,  $E_V$ ,  $E_P$ , and  $E_N$  are the energies of  $V_2PN$ , V, P, and N atoms in their substance, respectively. 4 is the number of atoms in the unit cell. The  $E_f$  was estimated as -0.29 eV/atom for monolayer  $V_2PN$ . Meanwhile, monolayer  $V_2PN$  in the FM state was dynamically stable with the absence of imaginary frequency in the phonon dispersion [see Fig. 2(d)]. Moreover, the MD simulation at 300 K showed that the final crystal lattice of monolayer  $V_2PN$  was maintained without structure frustration, indicating its thermal stability [see Fig. 2(e)]. As last, the calculated 2D effective elastic constants [see Table 1] satisfy the Born criteria [48] for 2D square lattice:  $C_{11} > 0$ ,  $C_{66} > 0$ , and  $C_{11} > -C_{12}$ , indicating its mechanical stability. Thus, monolayer  $V_2PN$  has good structural stability.

Liu et al. have recently reported the growth of monolayer VN on steel substrate via physical vapor deposition technology. [49] Cheng et al. proved that monolayer VP could be exfoliated from its bulk counterpart. [23] Similar to the experimental synthesis of Janus monolayer MoSSe [24] and WSSe, [25] one can replace one side of the P layer of monolayer VP with the N atoms or replace one side of the N layer of monolayer VN with the P atoms to prepare Janus monolayer  $V_2PN$ . V-N bonding is shorter and stronger than V-P bonding because of the larger electronegativity between V and N elements. Therefore, it is more favorable to prepare the Janus  $V_2PN$  from monolayer VP because the replacement of the P is an exothermic reaction.

The band structure of monolayer  $V_2PN$  is shown in Fig. 3(a). The spin-up bands cross the Fermi level while spin-down bands have a band gap. Thus, monolayer  $V_2PN$  is a half-metal. In the spin-down channel, the valence band maximum (VBM) and the conduction band minimum (CBM) are located at the M point and the  $\Gamma$  point of the Brillouin zone (BZ). The energy of the VBM is 1.02 eV lower than the Fermi level, which helps to prevent the thermally excited spin-flip transition. The more accurate HSE06 hybrid functional gave similar band structures [see Fig. S4(a)], indicating the



**Table 1.** Lattice constants  $a(\text{\AA})$ , bonding angle ( $^\circ$ ), and 2D effective elastic constants  $C_{ij}$  (N/m), the magnetocrystalline anisotropy (MCA), magnetic shape anisotropy (MSA) and MAE of monolayer  $V_2XN$  ( $X = P, As$ ). The unit of anisotropy energy is  $\mu\text{eV}$  per V atom.

	$a$	$\angle V-X-V$	$\angle V-N-V$	$C_{11}$	$C_{12}$	$C_{66}$	MCA	MSA	MAE
$V_2PN$	3.986	71.2	88.2	75.11	22.19	48.36	58.8	57.8	116.6
$V_2AsN$	3.989	67.6	88.3	73.28	21.53	44.87	230.8	61.2	292.0

rationality of  $U_f = 3$  eV in our work. The projected density of states (PDOS) near the Fermi level was mainly contributed by the  $d$ -orbitals of the V atoms [see Fig. S5]. Due to the  $C_{4V}$  symmetry, the  $p_x$  and  $p_y$  orbitals are degenerate. The  $d_{xz}$  and  $d_{yz}$  orbitals are degenerate. As shown in Fig. 3(b), the  $d_{x^2-y^2}$ ,  $d_{xz} + d_{yz}$ , and  $d_{xy}$  orbitals of the V atoms dominated the PDOS at the Fermi level in the spin-up channel. The  $d_{yz}$  and  $d_{xy}$  orbitals of the V atoms dominate the PDOS near the VBM and CBM in the spin-down channel, respectively. There is an effective overlap between the PDOS contributed by the  $d_{xz} + d_{yz}$  orbitals of V atoms and  $p_x + p_y$  orbitals of P and N atoms around the energy of -3 eV in the spin-up channel and -2 eV in the spin-down channel. The overlap between the PDOS contributed by the V- $d_{x^2-y^2}$  orbital and  $p_z$  orbitals of P and N atoms are also large in the same energy zone, as shown in Fig. S5. That indicated a strong  $p-d$  coupling between the V atom and the P or N atom, which stabilizes the square lattice of monolayer  $V_2PN$  and excludes the ferroelastic transition. [21]

A sizable MAE is significant to maintain magnetic ordering against heat fluctuation. There are two parts of contributions to the MAE. One is the magnetocrystalline anisotropy (MCA) energy ( $E_{MCA}$ ) due to the SOC effect, the other one is the magnetic shape anisotropy (MSA) energy ( $E_{MSA}$ ) due to the magnetic dipole-dipole interaction. Fig. 3(c) displayed the MCA of monolayer  $V_2PN$  in the whole space. The energy of monolayer  $V_2PN$  with magnetization along the in-plane direction is lower than that along the out-of-plane direction. Moreover, the energy difference of monolayer  $V_2PN$  with in-plane magnetization is less than  $0.01 \mu\text{eV}$  per V atom, thereby being regarded as isotropic in the  $xy$ -plane, as shown in Fig. 3(c). In the primitive cell, each V atom has a directional distribution of spin density. However, the spin density of two neighboring V atoms is orthogonal to each other [see the inset of Fig. 3(d)], which may lead to the in-plane isotropic magnetic properties. We determined the  $E_{MCA}$  of monolayer  $V_2PN$  by the energy difference between the system with magnetization along the  $z$ -direction and  $x$ -direction:  $E_{MCA} = E_z^{\text{soc}} - E_x^{\text{soc}}$ . As shown from Fig. 3(d), the  $E_{MCA}$  is  $58.8 \mu\text{eV}$  per V atom for monolayer  $V_2PN$ . The angular dependence of MCA can be expressed by [50]

$$E_{MCA}(\theta) = E_0 + K_1 \sin^2 \theta + K_2 \sin^4 \theta. \quad (1)$$

Here  $\theta$  is the azimuthal angle from the  $z$ -axis.  $E_0$  is a constant.  $K_1$  and  $K_2$  are the anisotropy constants. By fitting the  $E_{MCA}$  of  $xz$ -plane with Eq. 1,  $K_1$  and  $K_2$  were estimated as  $-58.805$  and  $0.003 \mu\text{eV}$  for monolayer  $V_2PN$ . The quadratic term in Eq. 1

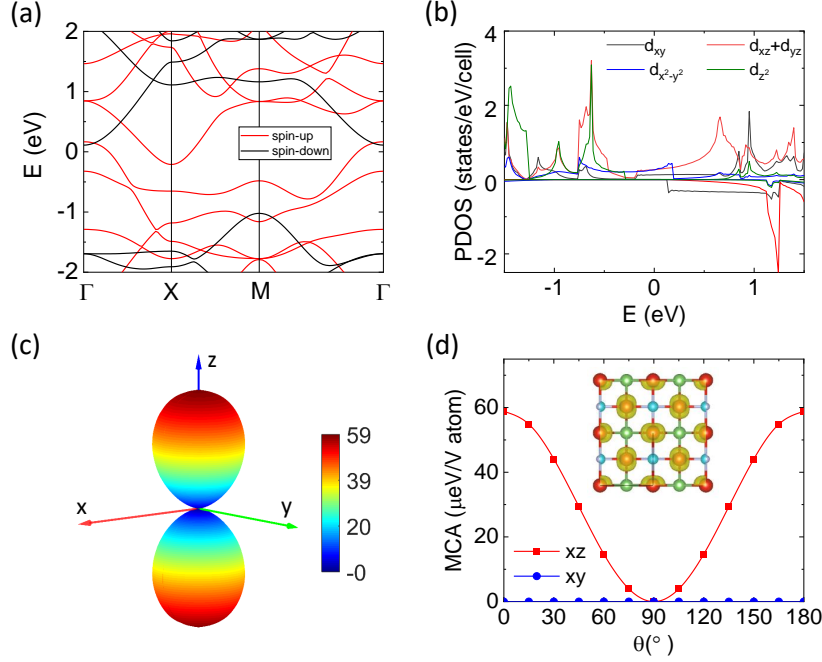


**Figure 3.** (a) band structure of monolayer V<sub>2</sub>PN. Red and black lines are spin-up and spin-down bands, respectively. (b) Projected density of states (PDOS) of monolayer V<sub>2</sub>PN. The positive and negative represent the PDOS in the spin-up and spin-down channels, respectively. (c) Angular dependence of the magnetocrystalline anisotropy (MCA) of monolayer V<sub>2</sub>PN with the direction of magnetization lying on the whole space, (d) The MCA of monolayer V<sub>2</sub>PN along different the orientations of magnetization in the  $xz$ - and  $xy$ -plane. The energy corresponding to the magnetization along the  $x$ -direction is set to be zero. The  $\theta$  is the azimuthal angle from the  $z$ -axis. The inset is the spin density with the isosurface as 0.03 eV/Å<sup>3</sup>.

dominates the MAE of monolayer V<sub>2</sub>PN.

The orbital-resolved MCA of monolayer V<sub>2</sub>PN was displayed in Fig. 4. The  $V-d$  orbitals make the main contribution to MCA. Based on the second-order perturbation theory, [51] the  $E_{MCA} = E_z^{\text{soc}} - E_x^{\text{soc}}$  can be expressed:

$$E_{MCA} = \xi^2(1 - 2\delta_{\alpha\beta}) \sum_{o,\alpha,u,\beta} \frac{|\langle o^\alpha | \hat{L}_z | u^\beta \rangle|^2 - |\langle o^\alpha | \hat{L}_x | u^\beta \rangle|^2}{\varepsilon_u^\alpha - \varepsilon_o^\beta}. \quad (2)$$

where  $\xi$ ,  $\hat{L}_{z(x)}$ ,  $\varepsilon_o$ , and  $\varepsilon_u$  are the SOC strength, angular momentum operators, the energy levels of occupied states and unoccupied states, respectively.  $\alpha$  and  $\beta$  are the spin index "+" and "-".  $\delta_{\alpha\beta}$  is 1 for  $\alpha = \beta$  and 0 for  $\alpha \neq \beta$ . The expression of  $E_{MCA}$  between our paper and original work [51] differs a minus due to the different definitions of  $E_{MCA}$ . Considering the denominator  $\varepsilon_u - \varepsilon_o$  of Eq. 2, the electronic states near the Fermi level dominate the MCA. Therefore, we did not consider the MCA from the contribution of the occupied state in the spin-down channel due to the large band gap. Meanwhile, the summation in Eq. 2 is related to the PDOS of occupied and unoccupied states. We classified the  $d$  orbitals by magnetic quantum number  $m$ . We used the  $d_{m=0}$ ,  $d_{|m|=1}$ , and  $d_{|m|=2}$  to represent  $d_{z^2}$ ,  $\{d_{xz}, d_{yz}\}$ , and  $\{d_{xy}, d_{x^2-y^2}\}$ , respectively. The matrix element



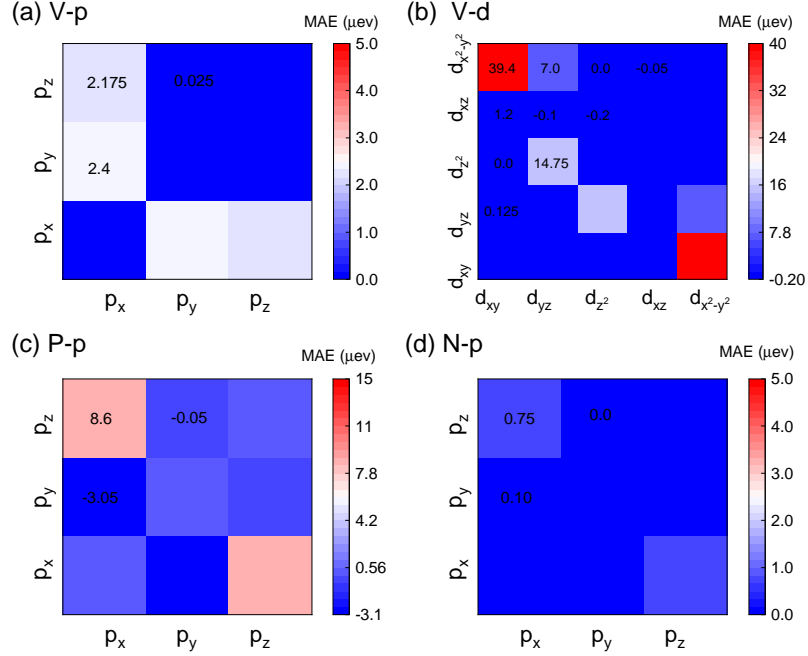


**Figure 4.** (a) Orbital-resolved MCA of the monolayer V<sub>2</sub>PN contributed by the hybridization between (a) the  $p$  orbitals of the V atoms, (b) the  $d$  orbitals of the V atoms, (c) the  $p$  orbitals of the P atoms, and (d) the  $p$  orbitals of the N atoms.

in the numerator of Eq. 2 is nonzero for  $\langle m | \hat{L}_z | m \rangle$  and  $\langle m | \hat{L}_x | m \pm 1 \rangle$ . Combining the Fig. 3(b) and 4(b), the  $E_{MCA}$  is mainly and positively contributed by  $\langle d_{x^2-y^2}^+ | \hat{L}_z | d_{xy}^- \rangle$  due to that the  $d_{xy}$  orbital in the CBM of spin-down bands is close to the Fermi level. The hybridization  $\langle d_{x^2-y^2}^+ | \hat{L}_x | d_{yz}^+ \rangle$  and  $\langle d_{z^2}^+ | \hat{L}_x | d_{yz}^+ \rangle$  also make positive contributions to the  $E_{MCA}$ . All these parts lead to a positive  $E_{MCA}$  for monolayer V<sub>2</sub>PN, which favors the in-plane magnetization of the V atom.

Compared to MCA, the magnetic dipole-dipole interaction usually favors the magnetization along the elongated direction of 1D or 2D materials.[52] We estimated the MSA energy  $E_{MSA} = E_z^{dipole} - E_x^{dipole}$  of monolayer V<sub>2</sub>PN with a classical magnetic dipole-dipole interaction model [see Fig. S6(a)]. The  $E_{MSA}$  is also positive, indicating that shape anisotropy also favors magnetization along the in-plane direction. Meanwhile, the  $E^{dipole}$  is isotropic in the  $xy$ -plane [see Fig. S6(b)]. Thus, the  $MAE = E_{MCA} + E_{MSA}$  of monolayer V<sub>2</sub>PN is isotropic in the  $xy$ -plane, indicating an easy magnetization  $xy$ -plane. Moreover, the mechanism of forming the easy-plane ferromagnetism in monolayer V<sub>2</sub>PN is different from monolayer CrCl<sub>3</sub>. Lu et al. have reported that the net effect of competition between the strong in-plane MSA and weak out-of-plane MCA leads to the easy magnetization plane of monolayer CrCl<sub>3</sub>. [14]

Compared to Janus monolayer V<sub>2</sub>PN, the  $E_{MCA}$  and  $E_{MSA}$  of monolayer VN are -140.1  $\mu\text{eV}$  per V atom and 36.9  $\mu\text{eV}$  per V atom, respectively [see Fig. S1(c)]. Thus, the MAE of monolayer VN is negative, indicating that monolayer VN exhibit an easy magnetization  $z$ -axis. Our result is contrasted with previous Kuklin's work, [46] due

to that we predicted a planar square lattice by PBE+U calculations while Kuklin et al. predicted a bucking square lattice by PBE calculations [46] [see Fig. S1 (a, b)]. The  $d_{|m|=1} = \{d_{xz}, d_{yz}\}$  orbitals in the spin-up channel dominated the PDOS around the Fermi level [see Fig. S1(c)]. The orbital-resolved MAE shows that the negative contribution of  $\langle d_{|m|=1}^+ | \hat{L}_z | d_{|m|=1}^+ \rangle$  is the main reason for the negative MCA of monolayer VN. As a result, the spins in monolayer VN prefers to be oriented along the  $z$ -direction through the normal FM phase transition.

Since Janus monolayer  $V_2PN$  is a 2D-XY ferromagnet, it will occur a BKT phase transition at low temperatures, [6] similar to monolayer  $CrCl_3$ . [14] Considering that a true spin is a 3D vector, we adopted the XXZ model to estimate the transition temperature  $T_{BKT}$ :

$$H = - \sum_{\langle i,j \rangle} [J_x(S_i^x S_j^x + S_i^y S_j^y) + J_z S_i^z S_j^z] - D \sum_i (S_i^z)^2, \quad (3)$$

where  $\mathbf{S}_i$  is the spin vector on site  $i$  and is normalized to 1.  $D$  is the single-ion anisotropy. We considered the exchange constants  $J$  up to the third nearest neighbors [see Fig. 2(b)]. The energy of the FM and AFM states with magnetization along the  $z$ -axis were expressed as

$$E_{FM}^z = E_0 - 2J_{1,z} - 2J_{2,z} - 2J_{3,z} - D, \quad (4)$$

$$E_{AFM1}^z = E_0 + 2J_{2,z} - 2J_{3,z} - D, \quad (5)$$

$$E_{AFM2}^z = E_0 + 2J_{1,z} - 2J_{2,z} - 2J_{3,z} - D, \quad (6)$$

$$E_{AFM3}^z = E_0 + 2J_{3,z} - D. \quad (7)$$

The energy corresponding to the magnetization along the  $x$ -axis can be obtained by replacing  $J_z$  by  $J_x$  and dropping the single-ion anisotropy  $D$  in above equations. We got eight equations to solve the exchange constants and single-ion anisotropy. The energies of different magnetic states can be obtained by first-principles calculations. By substituting the energies into Eq. 4 to 7, we obtained the  $J$  and  $D$ , as shown in Table 2. All the exchange constants are positive indicating the FM coupling between the V ions at different neighbors. The  $J_3$  is much smaller than  $J_1$  and  $J_2$ . The  $D$  is negative, which indicates that spins of V ions prefer to be in-plane rather than out-of-plane in monolayer  $V_2PN$ .

**Table 2.** The exchange constants  $J$  (meV) and single-ion anisotropy  $D$  (meV) of monolayer  $V_2PX$  (X = P, As).

	$J_{1,x}$	$J_{1,z}$	$J_{2,x}$	$J_{2,z}$	$J_{3,x}$	$J_{3,z}$	$D$
$V_2PN$	21.12	21.09	25.44	25.43	2.833	2.834	-0.007
$V_2AsN$	25.26	25.16	23.21	23.18	6.24	6.25	-0.008

We first made a qualitative estimation of  $T_{BKT}$  of monolayer  $V_2PN$ . With 2D square lattice with the nearest-neighboring exchange constant  $J_1$  being considered, the scaling

and renormalization-group calculations of XXZ model [53] gave the following form of  $T_{BKT}$ :

$$T_{BKT} = \frac{4\pi J_{1,x}}{A + \ln[(1 - \lambda)^{-1}]} \quad (8)$$

with  $\lambda = J_{1,z}/J_{1,x}$ . Cuccoli et al. predicted that the  $T_{BKT} = 0.546J_{1,x}/k_B$  for 2D square lattice with  $\lambda = 0.99$  by MC calculations.[54] So we could estimate the constant  $A$  in Eq.8 to be about 18.410. On the other side, Gouva et al. proposed that the  $T_{BKT}$  was scaled by  $(1 + 2J_2/J_1)$  by including the second nearest-neighboring exchange constant  $J_2$ . [55] By substituting the exchange constants from Table 2 into the Eq. 8, we predicted the  $T_{BKT}$  of monolayer  $V_2PN$  to be about 419.0 K which has exceeded the room temperature.

Next, we performed exact MC simulations. The out-of-plane averaged magnetic moments  $\langle M_z \rangle$  is much smaller than in-plane averaged magnetic moments  $\langle M_{xy} \rangle$  at any temperature [see Fig. 5(a)]. The in-plane magnetization exhibit a large fluctuation at low temperatures, which can be explained by the emergence of meron and antimeron spin textures. [14] The spin-spin correlation [14]  $C(r) = \langle \mathbf{S}(0) \cdot \mathbf{S}(r) \rangle$  of  $V_2PN$  occurs an exponential decay to zero at a high temperature (500 K) at which  $V_2PN$  is in the paramagnetic phase [see Fig. 5(b)]. At a low temperature (100 K),  $C(r)$  exhibits an algebraic decay continuously and indicates a quasi-long-range order through the BKT phase transition. [6]

The  $T_{BKT}$  can not be determined by specific heat  $C_V$  data as it displays not a divergence but a maximum value at a temperature above  $T_{BKT}$  for a 2D-XY ferromagnet. [56, 54] Cuccoli. et al [54] defined the susceptibility as the average of the squared magnetization,

$$\chi^{\alpha\alpha} = \frac{1}{N} \langle (\sum_{i=1}^N S_i^\alpha)^2 \rangle, \quad (9)$$

and in-plane susceptibility as  $\chi_{in} = (\chi^{xx} + \chi^{yy})/2$ . The  $N$  is the number of magnetic moments.  $\langle \dots \rangle$  denotes the time average of corresponding components. Such a definition of  $\chi_{in}$  retains its value in investigating the divergence of  $\chi_{in}$  also for finite lattice simulations. [54] It has been proved that  $\chi_{in}$  diverges exponentially as  $T_c$  is approached from above ( $T \rightarrow T_{BKT}^+$ ):

$$\chi_{in} \sim e^{b(T-T_{BKT})^{-1/2}}, \quad (10)$$

where  $b$  is a non-universal constant.  $\chi_{in}$  satisfies the form of

$$\chi_{in} \sim L^{2-\eta} \quad (11)$$

for  $T \leq T_{BKT}$ , where  $L$  is the size of the supercell. The exponent  $\eta$  is a function of temperature  $T$  and satisfies  $\eta = 1/4$  at  $T_{BKT}$ . [54]

We fitted the  $\chi_{in}$  with Eq. 10 and estimated the  $T_{BKT}$  of monolayer  $V_2PN$  to be about 395 K [see Fig. 5(c)], which is much higher than  $T_{BKT} = 12.95$  K of synthesized monolayer  $CrCl_3$ . [13, 14] To justify this prediction of  $T_{BKT}$ , we performed the MC simulations by supercells with different sizes  $L$ . We explored the finite-size scaling

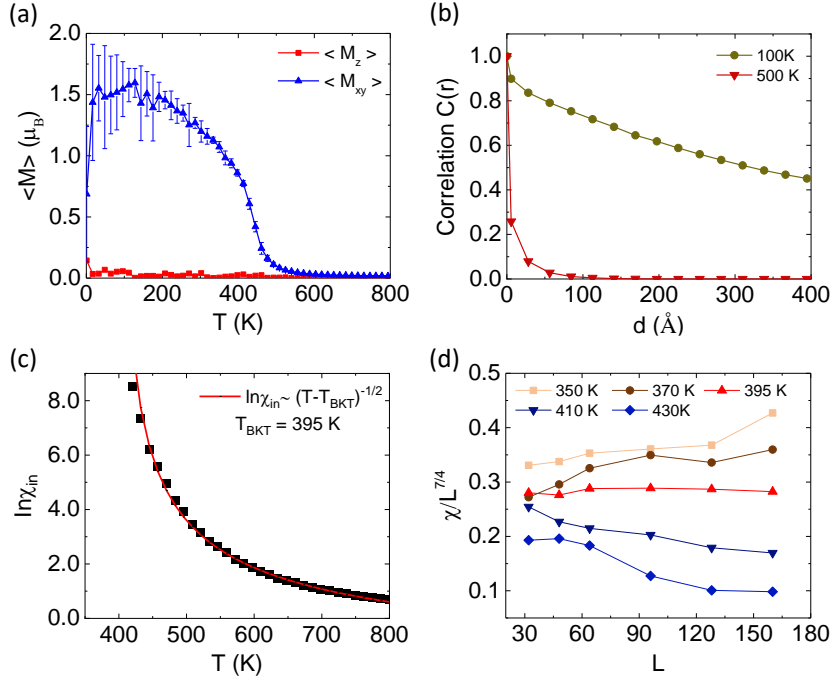


**Figure 5.** (a) Temperature dependence of averaged magnetization  $\langle M_{xy} \rangle$  and  $\langle M_z \rangle$  in monolayer  $V_2PN$ . The error bars are the standard deviation. (b) The spin-spin correlation function  $C(r)$  of in monolayer  $V_2PN$  at  $T = 100$  K and 500 K. (c) In-plane susceptibility  $\chi_{in}$  of monolayer  $V_2PN$  as a function of temperature. (e)  $\chi_{in}/L^{7/4}$  vs lattice size  $L$  of monolayer  $V_2PN$  at different temperatures.

behavior of in-plane susceptibility  $\chi_{in}$  by calculating the  $\chi_{in}/L^{7/4}$  as a function of supercell size  $L$ , as shown in Fig. 5(d). At  $T_{BKT} = 395$  K, the data  $\chi_{in}/L^{7/4}$  is insensitive to size  $L$ , indicating the behavior of  $\chi_{in} \sim L^{7/4}$ . That is consistent with the exponent  $\eta = 1/4$  at  $T_{BKT}$  [see Eq. 11]. [54] Meanwhile, the  $T_{BKT}$  is also consistent with the aforementioned rough estimation of  $T_{BKT}$  by the renormalization-group calculations [see Eq. 8]. [8] Thus, the estimation of  $T_{BKT}$  is reliable.

The representative real-space arrangement of magnetic moments after MC simulation is shown in Fig. 6 and Fig. S7 (a). The meron and antimeron spin textures were observed for temperature  $T < T_{BKT}$  [see Fig. 6(a)]. It was expected that the transport of these topological nontrivial spin textures is dispersionless at low temperatures, which can be applied in energy-efficient electronic devices. [14] The magnetic moments prefer to lie in-plane around spin defects but along the out-of-plane direction in the core of spin textures [see Fig. S7 (c ,d)], which is consistent with Wysin's prediction that perfect in-plane meron and antimeron is unstable and will develop out-of-plane spin component for 2D square lattices with  $\lambda = J_z/J_x > 0.704$ . [57] Actually, the  $\lambda$  has reached 0.99 for monolayer  $V_2PN$  [see Table 2]. As temperature increases, the spin structures of spin textures were disturbed by thermal energy. The number of merons or antimerons was decreased by thermal fluctuations [see Fig. 6(b) and Fig. S7(b)]. At  $T \geq T_{BKT}$ , we only observed the paramagnetic states.

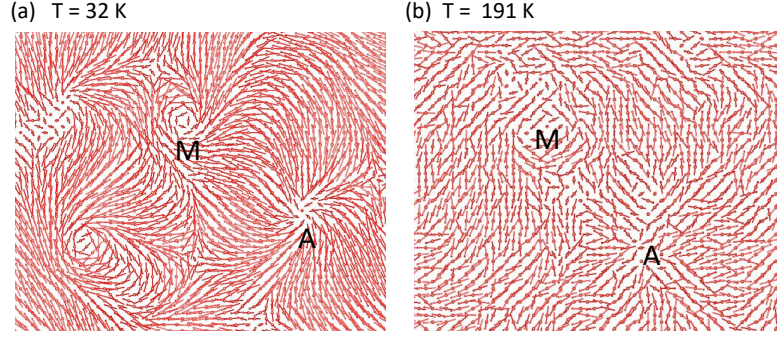


**Figure 6.** The top view of the real-space arrangement of magnetic moments of  $V_2PN$  after MC simulation at (a)  $T = 32$  K and (b)  $T = 191$  K. The length of the arrows represents the in-plane component of magnetic moments. The position of meron (M) and antimeron (A) are labeled.

We expanded the current calculations to monolayer  $V_2AsN$ . The FM state is the magnetic ground state for monolayer  $V_2AsN$  with  $U_f$  of  $2 \sim 4$  eV [see Fig. S2 (b) and S3 (b)]. The magnetic moments of the V, As, and N ions in a primitive cell are 2.236, -0.267, and -0.259  $\mu_B$ , respectively. Its formation energy  $E_f$  is -1.20 eV/atom. Its structural stability can be seen from the Fig. S2 (c, d) and Table 1. The electronic structures indicate that monolayer  $V_2AsN$  is also a half metal [see Fig. S2 (e, f) and S4 (b)]. The CBM of monolayer  $V_2AsN$  in the spin-down channel is more far away from the Fermi level than that of monolayer  $V_2PN$ . The estimation of MCA, MSA, MAE, exchange constants and  $T_{BKT}$  are shown in Fig. S6(a), Fig. S8 (a, b), Table 1 and Table 2. Due to the larger SOC effect, monolayer  $V_2AsN$  possesses a larger MAE of 292  $\mu eV$  per V atom, stronger exchange constants  $J$ , and a higher  $T_{BKT}$  of 434 K than that of monolayer  $V_2PN$ .

At last, we investigated the strain effect on the magnetic properties of monolayer  $V_2XN$  ( $X = P, As$ ). As the FM state has higher energy than AFM states at  $\varepsilon = -5\%$  [see Fig. 2(c)], we only varied the biaxial strain  $\varepsilon$  from -4% to 5%. We found that tensile strain increases the bond angles  $\angle V-X-V$  and  $\angle V-N-V$  in monolayer  $V_2XN$  ( $X = P, As$ ), making them closer to  $90^\circ$ . The FM coupling and the exchange constant  $J$  between V atoms was enhanced by tensile strain. As a result, the  $T_{BKT}$  of monolayer  $V_2PN$  and  $V_2AsN$  can be increased to 508.7 K and 531.3 K by a tensile strain of 5%, respectively. That is also consistent with the fact that the energy difference between FM and AFM states increases with tensile strain increasing [see Fig. 2(c)]. On the other side, the compressive strain has a negative influence on the exchange coupling between V atoms. The  $T_{BKT}$  of monolayer  $V_2PN$  and  $V_2AsN$  decreased quickly with the magnitude of compressive strain increasing. Compared to the  $T_{BKT}$ , the MAEs did not exhibit regular behavior with the temperatures changing. The  $E_{MSA}$  decreases as the distance between atoms increases, while the  $E_{MCA}$  has the opposite tendency [see Fig. S9]. Especially, the orbital resolved MAE shows that the contribution of hybridization

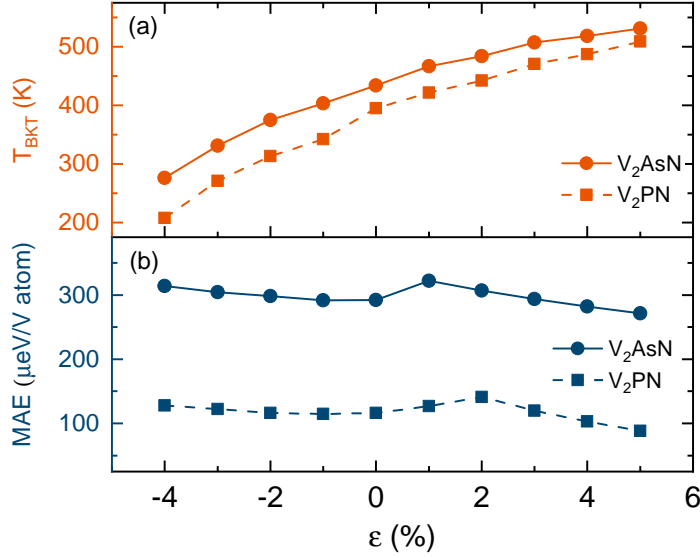


**Figure 7.** The (a) transition temperature  $T_{BKT}$  and (b) MAEs of monolayer  $V_2PN$  and  $V_2AsN$  as function of strain.

$\langle d_{x^2-y^2}^+ | \hat{L}_z | d_{xy}^- \rangle$  is the main reason for such a irregular behavior [see Fig. S9]. The MAE of monolayer  $V_2PN$  and  $V_2AsN$  ranges from  $271.3 \sim 321.9 \mu eV$  per V atom and  $88.5 \sim 141.1 \mu eV$  per V atom under strain ranging from -4% to 5%, respectively. In general, with a larger MAE and a higher  $T_{BKT}$ , monolayer  $V_2AsN$  is better than  $V_2PN$  for the material realization of the high-temperature 2D-XY ferromagnetism.

### 3.1. Acknowledgments

In summary, based on first-principles calculations, we systemically investigated the structural and magnetic properties of Janus monolayer  $V_2XN$  ( $X = P$  and  $As$ ). The strong electron correlation effect of  $d$  orbital of the V atoms was considered in both structure relaxation and electron structures. Monolayer  $V_2XN$  has a square lattice with good structural stability and FM half-metallic characters. The MAE is  $116.6 \mu eV/V$  atom and  $292.0 \mu eV/V$  atom for monolayer  $V_2PN$  and  $V_2AsN$ , respectively. Both the magnetocrystalline anisotropy and shape anisotropy favor an in-plane magnetization, leading to an easy magnetization  $xy$ -plane in monolayer  $V_2XN$ . MC simulations based on the 2D XXZ model indicated that monolayer  $V_2XN$  occurs the BKT phase transition with the emergence of topological non-trivial meron and antimeron spin textures. Through the analysis of the critical behavior of in-plane susceptibility, the  $T_{BKT}$  of monolayer  $V_2PN$  and  $V_2AsN$  was estimated as 395 K and 434 K, respectively. A 5% tensile strain can increase the corresponding  $T_{BKT}$  to 508.7 K and 531.3 K, respectively. Our work indicated that V-based Janus structures were candidate materials to realize the high-temperature 2D-XY ferromagnetism for spintronic applications.



- [1] Bevin Huang, Genevieve Clark, Efrén Navarro-Moratalla, Dahlia R. Klein, Ran Cheng, Kyle L. Seyler, Ding Zhong, Emma Schmidgall, Michael A. McGuire, David H. Cobden, Wang Yao, Di Xiao, Pablo Jarillo-Herrero, and Xiaodong Xu. Layer-dependent ferromagnetism in a van der waals crystal down to the monolayer limit. *Nature*, 546(7657):270–273, 2017.
- [2] Zaiyao Fei, Bevin Huang, Paul Malinowski, Wenbo Wang, Tiancheng Song, Joshua Sanchez, Wang Yao, Di Xiao, Xiaoyang Zhu, Andrew F. May, Weida Wu, David H. Cobden, Jiun-Haw Chu, and Xiaodong Xu. Two-dimensional itinerant ferromagnetism in atomically thin  $\text{Fe}_3\text{GeTe}_2$ . *Nat. Mater.*, 17(9):778–782, 2018.
- [3] Cheng Gong, Lin Li, Zhenglu Li, Huiwen Ji, Alex Stern, Yang Xia, Ting Cao, Wei Bao, Chenzhe Wang, Yuan Wang, Z. Q. Qiu, R. J. Cava, Steven G. Louie, Jing Xia, and Xiang Zhang. Discovery of intrinsic ferromagnetism in two-dimensional van der waals crystals. *Nature*, 546(7657):265–269, 2017.
- [4] Dante J. O’Hara, Tiancong Zhu, Amanda H. Trout, Adam S. Ahmed, Yunqiu Kelly Luo, Choong Hee Lee, Mark R. Brenner, Siddharth Rajan, Jay A. Gupta, David W. McComb, and Roland K. Kawakami. Room temperature intrinsic ferromagnetism in epitaxial manganese selenide films in the monolayer limit. *Nano Lett.*, 18(5):3125–3131, 2018.
- [5] Manuel Bonilla, Sadhu Kolekar, Yujing Ma, Horacio Coy Diaz, Vijaysankar Kalappattil, Raja Das, Tatiana Eggers, Humberto R. Gutierrez, Manh-Huong Phan, and Matthias Batzill. Strong room-temperature ferromagnetism in  $\text{VSe}_2$  monolayers on van der waals substrates. *Nat. Nanotechnol.*, 13(4):289–293, 2018.
- [6] J M Kosterlitz and D J Thouless. Ordering, metastability and phase transitions in two-dimensional systems. *J. Phys. C*, 6(7):1181–1203, apr 1973.
- [7] J M Kosterlitz. The critical properties of the two-dimensional xy model. *J. Phys. C: Solid State Phys.*, 7(6):1046, mar 1974.
- [8] Jiesu Wang. Berezinskii-kosterlitz-thouless phase transition in a 2D-XY ferromagnetic monolayer. *J. Semicond.*, 42(12):120401, dec 2021.
- [9] Andrey M. Tokmachev, Dmitry V. Averyanov, Alexander N. Taldenkov, Ivan S. Sokolov, Igor A. Karateev, Oleg E. Parfenov, and Vyacheslav G. Storchak. Two-dimensional magnets beyond the monolayer limit. *ACS Nano*, 15(7):12034–12041, 2021.
- [10] Ivan S. Sokolov, Dmitry V. Averyanov, Oleg E. Parfenov, Igor A. Karateev, Alexander N. Taldenkov, Andrey M. Tokmachev, and Vyacheslav G. Storchak. 2D ferromagnetism in europium/graphene bilayers. *Mater. Horiz.*, 7(5):1372–1378, 2020.
- [11] Andrey M. Tokmachev, Dmitry V. Averyanov, Oleg E. Parfenov, Alexander N. Taldenkov, Igor A. Karateev, Ivan S. Sokolov, Oleg A. Kondratev, and Vyacheslav G. Storchak. Emerging two-dimensional ferromagnetism in silicene materials. *Nat. Commun.*, 9(1):1672, 2018.
- [12] Andrey M. Tokmachev, Dmitry V. Averyanov, Alexander N. Taldenkov, Oleg E. Parfenov, Igor A. Karateev, Ivan S. Sokolov, and Vyacheslav G. Storchak. Lanthanide  $f^7$  metalloxenes - a class of intrinsic 2D ferromagnets. *Mater. Horiz.*, 6(7):1488–1496, 2019.
- [13] Amilcar Bedoya-Pinto, Jing-Rong Ji, Avanindra K. Pandeya, Pierluigi Gargiani, Manuel Valvidares, Paolo Sessi, James M. Taylor, Florin Radu, Kai Chang, and Stuart S. P. Parkin. Intrinsic 2D-XY ferromagnetism in a van der waals monolayer. *Science*, 374(6567):616–620, oct 2021.
- [14] Xiaobo Lu, Ruixiang Fei, Linghan Zhu, and Li Yang. Meron-like topological spin defects in monolayer  $\text{CrCl}_3$ . *Nat. Commun.*, 11(1):4724, 2020.
- [15] Mathias Augustin, Sarah Jenkins, Richard F. L. Evans, Kostya S. Novoselov, and Elton J. G. Santos. Properties and dynamics of meron topological spin textures in the two-dimensional magnet  $\text{CrCl}_3$ . *Nat. Commun.*, 12(1):185, 2021.
- [16] Mara Strungaru, Mathias Augustin, and Elton J. G. Santos. Ultrafast laser-driven topological spin textures on a 2d magnet. *npj Comput. Mater.*, 8(1):169, 2022.
- [17] An-Ning Ma, Pei-Ji Wang, and Chang-Wen Zhang. Intrinsic ferromagnetism with high temperature, strong anisotropy and controllable magnetization in the  $\text{CrX}$  ( $\text{X} = \text{P}, \text{As}$ )

- monolayer. *Nanoscale*, 12:5464–5470, 2020.
- [18] Qirui Cui, Yingmei Zhu, Jinghua Liang, Ping Cui, and Hongxin Yang. Spin-valley coupling in a two-dimensional  $\text{VS}_2\text{iN}_4$  monolayer. *Phys. Rev. B*, 103(8):085421, feb 2021.
  - [19] Michael Ashton, Dorde Gluhovic, Susan B. Sinnott, Jing Guo, Derek A. Stewart, and Richard G. Hennig. Two-dimensional intrinsic half-metals with large spin gaps. *Nano Lett.*, 17(9):5251–5257, 2017.
  - [20] Julio F. Fernández, Manuel F. Ferreira, and Jolanta Stankiewicz. Critical behavior of the two-dimensional XY model: A monte carlo simulation. *Phys. Rev. B*, 34:292–300, Jul 1986.
  - [21] Xiaoyu Xuan, Wanlin Guo, and Zhuhua Zhang. Ferroelasticity in two-dimensional tetragonal materials. *Phys. Rev. Lett.*, 129:047602, Jul 2022.
  - [22] Xiaoyu Xuan, Menghao Wu, Zhuhua Zhang, and Wanlin Guo. A multiferroic vanadium phosphide monolayer with ferromagnetic half-metallicity and topological dirac states. *Nanoscale Horiz.*, 7:192–197, 2022.
  - [23] Xuli Cheng, Shaowen Xu, Fanhao Jia, Guodong Zhao, Minglang Hu, Wei Wu, and Wei Ren. Intrinsic ferromagnetism with high curie temperature and strong anisotropy in a ferroelastic VX monolayer (X=P, As). *Phys. Rev. B*, 104:104417, 2021.
  - [24] Ang-Yu Lu, Hanyu Zhu, Jun Xiao, Chih-Piao Chuu, Yimo Han, Ming-Hui Chiu, Chia-Chin Cheng, Chih-Wen Yang, Kung-Hwa Wei, Yiming Yang, Yuan Wang, Dimosthenis Sokaras, Dennis Nordlund, Peidong Yang, David A. Muller, Mei-Yin Chou, Xiang Zhang, and Lain-Jong Li. Janus monolayers of transition metal dichalcogenides. *Nat. Nanotechnol.*, 12(8):744–749, 2017.
  - [25] Yu-Chuan Lin, Chenze Liu, Yiling Yu, Eva Zarkadoula, Mina Yoon, Alexander A. Puretzy, Liangbo Liang, Xiangru Kong, Yiyi Gu, Alex Strasser, Harry M. Meyer, Matthias Lorenz, Matthew F. Chisholm, Ilia N. Ivanov, Christopher M. Rouleau, Gerd Duscher, Kai Xiao, and David B. Geohegan. Low energy implantation into transition-metal dichalcogenide monolayers to form Janus structures. *ACS Nano*, 14(4):3896–3906, 2020.
  - [26] Dipesh B. Trivedi, Guven Turgut, Ying Qin, Mohammed Y. Sayyad, Debarati Hajra, Madeleine Howell, Lei Liu, Sijie Yang, Naim Hossain Patoary, Han Li, Marko M. Petrić, Moritz Meyer, Malte Kremser, Matteo Barbone, Giancarlo Soavi, Andreas V. Stier, Kai Müller, Shize Yang, Ivan Sanchez Esqueda, Houlong Zhuang, Jonathan J. Finley, and Sefaattin Tongay. Room-temperature synthesis of 2D Janus crystals and their heterostructures. *Adv. Mater.*, 32(50):2006320, 2020.
  - [27] LuoJun Du, Tawfique Hasan, Andres Castellanos-Gomez, Gui-Bin Liu, Yugui Yao, Chun Ning Lau, and Zhipei Sun. Engineering symmetry breaking in 2D layered materials. *Nat. Rev. Phys.*, 3(3):193–206, 2021.
  - [28] Fang Zhang, Wenbo Mi, and Xiaocha Wang. Spin-dependent electronic structure and magnetic anisotropy of 2D Ferromagnetic Janus  $\text{Cr}_2\text{I}_3\text{X}_3$  (X = Br, Cl) monolayers. *Adv. Electron. Mater.*, 6(1):1900778, 2020.
  - [29] Rui Li, Jiawei Jiang, Xiaohui Shi, Wenbo Mi, and Haili Bai. Two-dimensional janus  $\text{FeXY}$  (X, Y = Cl, Br, and I) monolayers: Half-metallic ferromagnets with tunable magnetic properties under strain. *ACS Appl. Mater. Interfaces*, 13(32):38897–38905, 2021. PMID: 34370461.
  - [30] Rui Li, Jiawei Jiang, Wenbo Mi, and Haili Bai. Ferroelectric polarization tailored interfacial charge distribution to modify magnetic properties of two-dimensional Janus  $\text{FeBrI}/\text{In}_2\text{S}_3$  heterostructures. *Appl. Phys. Lett.*, 120(16):162401, 2022.
  - [31] Rui Li, Jiawei Jiang, Wenbo Mi, and Haili Bai. Room temperature spontaneous valley polarization in two-dimensional  $\text{FeClBr}$  monolayer. *Nanoscale*, 13:14807–14813, 2021.
  - [32] Changsong Xu, Junsheng Feng, Sergei Prokhorenko, Yousra Nahas, Hongjun Xiang, and L. Bellaiche. Topological spin texture in Janus monolayers of the chromium trihalides  $\text{Cr}(\text{I}, \text{X})_3$ . *Phys. Rev. B*, 101(6):060404(R), 2020.
  - [33] Jiaren Yuan, Yumeng Yang, Yongqing Cai, Yihong Wu, Yuanping Chen, Xiaohong Yan, and Lei Shen. Intrinsic skyrmions in monolayer Janus magnets. *Phys. Rev. B*, 101(9):094420, 2020.
  - [34] Dibyendu Dey and Antia S. Botana. Structural, electronic, and magnetic properties of vanadium-

- based Janus dichalcogenide monolayers: A first-principles study. *Phys. Rev. Mater.*, 4(7):074002, 2020.
- [35] G. Kresse and J. Furthmüller. Efficient iterative schemes for ab initio total-energy calculations using a plane-wave basis set. *Phys. Rev. B*, 54:11169–11186, 1996.
  - [36] G. Kresse and D. Joubert. From ultrasoft pseudopotentials to the projector augmented-wave method. *Phys. Rev. B*, 59:1758–1775, 1999.
  - [37] John P. Perdew, Kieron Burke, and Matthias Ernzerhof. Generalized gradient approximation made simple. *Phys. Rev. Lett.*, 77:3865–3868, 1996.
  - [38] Hendrik J. Monkhorst and James D. Pack. Special points for brillouin-zone integrations. *Phys. Rev. B*, 13:5188–5192, 1976.
  - [39] S. L. Dudarev, G. A. Botton, S. Y. Savrasov, C. J. Humphreys, and A. P. Sutton. Electron-energy-loss spectra and the structural stability of nickel oxide: An LSDA+U study. *Phys. Rev. B*, 57:1505–1509, Jan 1998.
  - [40] W. E. Pickett, S. C. Erwin, and E. C. Ethridge. Reformulation of the LDA+U method for a local-orbital basis. *Phys. Rev. B*, 58:1201–1209, Jul 1998.
  - [41] Y. K. Wang, P. H. Lee, and G. Y. Guo. Half-metallic antiferromagnetic nature of  $\text{La}_2\text{VTcO}_6$  and  $\text{La}_2\text{VCuO}_6$  from ab initio calculations. *Phys. Rev. B*, 80:224418, Dec 2009.
  - [42] F. Aryasetiawan, K. Karlsson, O. Jepsen, and U. Schönberger. Calculations of hubbard U from first-principles. *Phys. Rev. B*, 74:125106, Sep 2006.
  - [43] Jochen Heyd, Gustavo E. Scuseria, and Matthias Ernzerhof. Hybrid functionals based on a screened coulomb potential. *J. Chem. Phys.*, 118(18):8207–8215, 2003.
  - [44] Atsushi Togo and Isao Tanaka. First principles phonon calculations in materials science. *Scr. Mater.*, 108:1–5, 2015.
  - [45] Liang Liu, Xue Ren, Jihao Xie, Bin Cheng, Weikang Liu, Taiyu An, Hongwei Qin, and Jifan Hu. Magnetic switches via electric field in BN nanoribbons. *Appl. Surf. Sci.*, 480:300–307, jun 2019.
  - [46] Artem V. Kuklin, Svetlana A. Shostak, and Alexander A. Kuzubov. Two-dimensional lattices of VN: Emergence of ferromagnetism and half-metallicity on nanoscale. *J. Phys. Chem. Lett.*, 9(6):1422–1428, 2018. PMID: 29502418.
  - [47] John B. Goodenough. Theory of the role of covalence in the perovskite-type manganites  $[\text{La}, \text{M(II)}]\text{MnO}_3$ . *Phys. Rev.*, 100(2):564–573, oct 1955.
  - [48] Marcin Maździarz. Comment on ‘the computational 2D materials database: high-throughput modeling and discovery of atomically thin crystals’. *2D Materials*, 6(4):048001, jul 2019.
  - [49] Z.X. Liu, Yong Li, X.H. Xie, Jun Qin, and Y. Wang. The tribo-corrosion behavior of monolayer VN and multilayer VN/C hard coatings under simulated seawater. *Ceram. Int.*, 47(18):25655–25663, 2021.
  - [50] K. H. J. Buschow and F. R. de Boer. *Physics of Magnetism and Magnetic Materials*. Springer US, 2003.
  - [51] Ding sheng Wang, Ruqian Wu, and A. J. Freeman. First-principles theory of surface magnetocrystalline anisotropy and the diatomic-pair model. *Phys. Rev. B*, 47(22):14932–14947, jun 1993.
  - [52] David C. Johnston. Magnetic dipole interactions in crystals. *Phys. Rev. B*, 93:014421, Jan 2016.
  - [53] K.H. Fischer. Kosterlitz-thouless transition in layered high- $T_c$  superconductors. *Physica C: Superconductivity*, 210(1):179–187, 1993.
  - [54] Alessandro Cuccoli, Valerio Tognetti, and Ruggero Vaia. Two-dimensional XXZ model on a square lattice: A monte carlo simulation. *Phys. Rev. B*, 52:10221–10231, Oct 1995.
  - [55] M. E. Gouvêa and A. S. T. Pires. The two dimensional classical anisotropic heisenberg ferromagnetic model with nearest- and next-nearest neighbor interactions. *Eur. Phys. J. B*, 25(2):147–153, 2002.
  - [56] Rajan Gupta and Clive F. Baillie. Critical behavior of the two-dimensional XY model. *Phys. Rev. B*, 45:2883–2898, Feb 1992.
  - [57] G. M. Wysin. Instability of in-plane vortices in two-dimensional easy-plane ferromagnets. *Phys.*

*Rev. B*, 49:8780–8789, Apr 1994.